Crop specific green area index retrieval from MODIS data at regional scale by controlling pixel-target adequacy

Grégory Duveiller, Frédéric Baret, Pierre Defourny

Crop specific green area index retrieval from MODIS data at regional scale by controlling pixel–target adequacy

Grégory Duveiller[a,*], Frédéric Baret[b], Pierre Defourny[a]

[a] *Earth and Life Institute, Université Catholique de Louvain, 2/16 Croix du Sud, B-1348 Louvain-la-Neuve, Belgium*
[b] *Environnement Méditerranéen et Modélisation des Agro-Hydrosystèmes (EMMAH), INRA-UMR 1114, Domaine Saint-Paul, Site Agroparc, 84914 Avignon, France*

Abstract

Information on vegetation status can be retrieved from satellite observations by modelling and inverting canopy radiative transfer. Agricultural monitoring and yield forecasting could greatly benefit from such techniques by coupling crop growth models with crop specific information through data assimilation. An indicator which would be particularly interesting to obtain from remote sensing is the total surface of photosynthetically active plant tissue, or Green Area Index (GAI). Currently, the major limitation is that the imagery that can be used operationally and economically over large areas with high temporal frequency have a coarse spatial resolution. This paper demonstrates how it is possible to characterize the regional crop specific GAI range along with its temporal dynamic using MODIS imagery by controlling the degree at which the observation footprints of the coarse pixels fall within the crop-specific mask delineating the target. This control is done by modelling the instrument's point spread function and by filtering out less reliable GAI estimations in both the spatial and temporal dimensions using thresholds on 3 variables: pixel purity, observation coverage and view zenith angle. The difference in performance between MODIS and fine spatial resolution to estimate the median GAI of a given crop over a 40×40 km study region can be reduced to a RMSE of 0.053 m^2/m^2. The consistency between fine and coarse spatial resolution GAI estimations suggest a possible instrument synergy whereby the high temporal

*Corresponding author currently at Institute for Environment and Sustainability, European Commission - Joint Research Centre, Via Fermi 2749, Ispra, Varese, Italy. Tel: +39 033278 9161. Fax: +39 033278 3033

Email addresses: gregory.duveiller@jrc.ec.europa.eu (Grégory Duveiller), frederic.baret@avignon.inra.fr (Frédéric Baret), pierre.defourny@uclouvain.be (Pierre Defourny)

resolution of MODIS provides the general GAI trajectory and while high spatial resolution can be used to estimate the local GAI spatial heterogeneity.

Keywords: Green area index, leaf area index, canopy radiative transfer, crop growth monitoring, regional scale, MODIS, pixel purity, observation coverage, Point Spread Function

1. Introduction

Monitoring vegetation dynamics over the Earth's surface is of paramount importance for agricultural, hydrological, meteorological and climate applications. The surface of green foliage is the main interface between atmosphere and vegetation, thereby governing the exchanges of energy, water and carbon. Both the radiative transfer and the functioning of a vegetation canopy are driven by the leaf area index (LAI), defined as half the total developed area of green leaves per unit of ground horizontal surface area (Chen & Black, 1992). LAI is a state variable in various land surface models, and more specifically in crop growth models (e.g. CERES (Ritchie & Otter, 1985), WOFOST (van Diepen et al., 1989) and STICS (Brisson et al., 1998)). Providing an estimation of such biophysical variables at relevant spatial and temporal resolutions can assist and potentially improve modelling approaches by either forcing the model or by controlling its temporal trajectory using assimilation techniques (Moulin et al., 1998; Cayrol et al., 2000; Dorigo et al., 2007).

Earth observation from satellite remote sensing provides synoptic and timely coverage which can be used to derive land surface variables such as LAI over large geographic extents. It is however necessary to characterize and invert the complex and non-linear relationship between canopy structure and reflectance (Myneni et al., 1995). For crops such as cereals in which all main aerial plant organs (leaves, stems, ears) are green and photosynthetically active, it is more appropriate to use the term of green area index (GAI) to refer to the biophysical variable retrieved from remote sensing since the radiance measured by the instrument is made of electromagnetic radiation reflected from all plant organs

(Duveiller et al., 2011). While estimating such information on canopy status at field level from high spatial resolution imagery has been done throughout the past decades with increasing performances, a real challenge is to estimate it over large geographical extents. LAI datasets have been produced at global scale (*e.g.* Sellers et al., 1994; Los et al., 2000; Myneni et al., 2002; Masson et al., 2003; Deng et al., 2006; Baret et al., 2007) but their spatial resolution (at best 1 km) is much too coarse to be crop specific over many landscapes across the world.

Satellite remote sensing is intrinsically confronted to a trade-off between spatial, temporal, spectral and radiometric resolutions. The high observation frequency necessary to detect anomalies due to climatic variability comes at the expense of coarser observation supports, which in turn results in measuring a signal originating from a larger and potentially more heterogeneous area. Although technological improvements are bound to provide finer spatial resolution data with more frequent observations, coarse instruments will retain a valuable interest since they provide a long time record. Medium or moderate spatial resolution instruments, best represented by MODIS on-board of Terra and Aqua platforms(Salomonson et al., 1989), MERIS on-board of ENVISAT (Rast et al., 1999) and the forthcoming OLCI which will be on-board of the GMES Sentinel-3 platform (Nieke et al., 2008), offer an interesting combination of spatial and spectral resolutions with high temporal repetitivity. However, given their spatial resolutions (pixel size ranging from around 250 to 500 m), it is still required to address the issue of spatial heterogeneity in order to have crop specific information over many agricultural landscapes around the world.

Large uncertainties arise when the reflectance encoded by a pixel originates either from a mixture of different land covers or from a single land cover with spatially heterogeneous properties. Intra-pixel spatial heterogeneity biases the estimation of land surface variables, such as LAI, when the relationship between this variable and the radiometric signal is non-linear (Friedl et al., 1995; Garrigues et al., 2006a). Geostatistics, and more precisely variograms, can be used to quantify landscape spatial heterogeneity from concurrent fine spatial resolu-

tion imagery (Garrigues et al., 2006b), providing the necessary information to correct the bias on the non-linear estimation of LAI (Garrigues et al., 2006a). The temporal changes in spatial heterogeneity can even be modelled to reduce the limitation of requiring concurrent imagery (Garrigues et al., 2008). Another approach for monitoring heterogeneous landscapes is to downscale coarse spatial resolution time series using unmixing-based data fusion (Zurita-Milla et al., 2009), thus creating fine spatial resolution synthetic images from which biophysical variables can be retrieved. A common disadvantage of both methods (correcting the scaling bias and downscaling) is that they require a series of fine spatial resolution imagery, preferably during the increasing phase of LAI which unfortunately often coincides with the rainy season in many part of the world. Furthermore, modelling the spatial heterogeneity with these methods can be a complex issue, requiring serious approximations and *a priori* knowledge which might not be readily available for operational application.

Both above-mentioned approaches provide elegant solutions to deal with intra-pixel heterogeneity in order to provide a spatially exhaustive coverage of land surface variable estimations from coarse spatial resolution data. However, their sophistication potentially induces more approximation errors, which can be avoided if spatially continuous maps are not mandatory. Rather than using all the pixels in a scene, the analysis can be restricted to a subset of a region's pixels (Guissard et al., 2004; Kastens et al., 2005). Masking the cropland can significantly improve the accuracy of crop yield forecasts based on NDVI profiles (Genovese et al., 2001). But crop growth models are often specific to a given crop (or crop variety), and in order to couple them with remote sensing data it is preferable to use crop-specific masking. In some landscapes, like the north China plains, this is trivial since more than 90% of arable lands are covered by wheat during spring (Ren et al., 2008). Many landscapes are more fragmented: a crop specific field will be surrounded by other crops, and it is complicated to anticipate the patterns due to crop rotation. Furthermore, the size of a medium spatial resolution pixel is often, at best, of the same order of magnitude as the size of crop fields. In order to make proper use of medium resolution data

for crop growth monitoring, it is required to select pixels whose observational footprints fall within the target crop specific fields. A common misconception is that the observational footprint is the geometric projection of a rectangular pixel onto the Earth's surface (Cracknell, 1998). The footprint rather depends on the instrument's point spread function (PSF), which describes how the electromagnetic radiation coming from a point source is spread over the image plane as it is recorded by the imaging instrument. Duveiller & Defourny (2010) demonstrated how modelling the PSF and convolving it over a crop specific mask can yield a pixel purity map. This maps provides the crop specific pixel purity (π), a variable defining the proportion of signal encoded in a pixel which orginates from the targeted crop.

The objective of this paper is to demonstrate whether it is possible to estimate both the spatial range and temporal dynamic of crop specific GAI at regional scale from medium spatial resolution data. Regional scale is here understood as a situation when the extent of the geographic coverage should be national or sub-national and the elementary unit of interest is a small area with similar agro-ecological growing conditions (preferably with an administrative delineation in order to link results to official statistics). This paper targets the population of all fields of a given crop within one such area, in which GAI is expected to vary due to differences in soil types, management practices, crop varieties, etc. despite being subject to the similar local weather. The characterisation of the GAI of this population with medium resolution imagery will be achieved by controlling the adequacy between observation footprint and the targeted fields using pixel purity. The impact of the selection of pixel purity thresholds on the characterization of the regional GAI will first be studied. A second analysis will then focus on how the observation geometry can further be used to filter out GAI estimations of lower quality to improve the temporal consistency of the GAI profiles. Finally, the results are validated using GAI maps obtained from high spatial resolution imagery acquired at various dates along the growing season.

2. Study site and data

To achieve the above-mentionned objectives, both fine and coarse spatial resolution imagery needs to be available over a large agricultural landscape along the whole growing season. The chosen study site is 40 × 40 km in size and is located in the Danube Plain, centred on Fundulea (Romania, around 44.41° N, 26.58° E). This agricultural landscape is dominated by relatively large fields (15 to 40 ha) of winter cereals (wheat and barley) alternating with summer crops (such as maize and sunflower). In 2001, imagery over the study site was intensely collected by high spatial resolution SPOT satellites thanks to a project called ADAM (Assimilation of spatial Data within Agronomic Models), whose aim was to develop and evaluate methods capable of exploiting high spatial satellite observations to optimize cultural practices, estimate the production, and evaluate environment impacts (Baret et al., 2001). The SPOT imagery in the ADAM dataset[1] constitutes the high spatial resolution data used in this paper, while the coarse spatial resolution data are assured by MODIS imagery.

2.1. SPOT imagery

The imagery within the ADAM dataset is composed of a time series of cloud-free images acquired from the SPOT 1, 2 and 4 satellites. The two HRV (High Resolution Visible) instruments on-board of the SPOT 1 and 2 platforms measure radiance in the green, red and near-infrared domain (NIR). The two HRVIR (High Resolution Visible InfraRed) instruments on-board of the SPOT 4 platform have an extra band which measures shortwave infrared wavelengths (SWIR). All images have a 20 m nominal ground sampling distance. The images have been accurately calibrated both radiometrically and geometrically by CNES (Centre National d'Etudes Spatiales, Toulouse, France). Both top-of-atmosphere (TOA) and top-of-canopy (TOC) reflectance imagery are available, the atmospheric correction having been done with the SMAC model (Rahman

[1] All the data is available at http://kalideos.cnes.fr/

& Dedieu, 1994) using aerosol characteristics measured with an automated sun-photometer on the ground. For the present experiment, a subset of 16 TOC reflectance images are used. These are distributed along the winter wheat growing season between DoY (day-of-year) 60 and DoY 180. Table 1 presents the characteristics of the selected images, including the type of instrument and acquisition geometry *i.e.* view zenith angles (VZA), sun zenith angles (SZA) and relative azimuth angles (RAA).

[Table 1 about here.]

2.2. MODIS imagery

MODIS provides observation in 36 spectral bands: 29 bands with a spatial resolution at nadir close to 1 km, 5 bands with a spatial resolution close to 500 m and 2 bands with a spatial resolution close to 250 m.[2] MODIS scans the Earth with a 2340 km swath, providing a global coverage every 1-2 days. MODIS data has the great advantage of being pre-processed, free and readily available to the scientific community from the NASA Distributed Active Archive Center[3]. The MODIS data used in this paper are the daily reflectance data at 250 m of spatial resolution for which 2 bands are available encoding reflectance respectively in the red and near-infrared spectral domains. This data are known as MOD09 and are part of collection 5 products. These level 2 products are all stored in the same grid, known as the L2G grid (see Wolfe et al., 1998, for details). In this grid, the is data is projected using a Sinusoidal projection with a specific spheroid (a sphere with a radius of 6371007.181 m), and is distributed by tiles of 4800 × 4800 pixels.

MODIS has some specific observational characteristics (see figure 1) that must be taken into account when studying ground objects which are close to

[2]Although MODIS products are generally referred to as having 1 km, 500 m and 250 m spatial resolution, the actual values are smaller and correspond respectively to 30, 15 and 7.5 arcseconds of the spheroid.

[3]https://wist.echo.nasa.gov/api/

the pixel size. MODIS is a whiskbroom scanner whose integration time as the rotating mirror scans the Earth is nearly a whole detector width (Schowengerdt, 2007) causing much higher spatial inter-pixel correlation in the cross-track direction than in the along-track direction. Furthermore, the MODIS pre-processing step of gridding, *i.e.* assigning an observation to a predefined system of grid, introduces a "pixel-shift" (Wolfe et al., 1998). This shift can be quantitatively described by the notion of "observation coverage" or *obscov* (Wolfe et al., 1998) which is a ratio between: (1) the intersection area between the nominal observation and the grid cell; and (2) the nominal area of the observation. The distribution of *obscov* values across a tile varies with the revisit cycle (figure 2). Tan et al. (2006) used this *obscov* value, which is provided along with MODIS reflectance products, to show the impact that gridding artifacts may have on compositing and band-to-band registration of MODIS data. These problems are compounded by the large across-track scan angle range of MODIS which results in view zenith angles (VZA) that can reach 65°. As the view zenith angle increases, so does the surface observed by the detector. This jeopardizes the quality of MODIS data since: (i) consecutive scan lines overlap when the VZA is different from 0° (the so-called "bow-tie" effect (Wolfe et al., 2002)) causing discontinuities of the latitude/longitude fields provided with the data (Khlopenkov & Trishchenko, 2008); and (ii) with a high VZA, individual observations cover several adjacent grid cells since the grid cell size is fixed throughout the image. Since the nominal area of the observation defining *obscov* increases with VZA, both variables are not independent. However they provide information at different levels. Depending on how the observations will be positioned with respect to the grid, some observations with high VZA have higher *obscov* than their neighbours and can therefore be considered as more reliable. Similarly, low VZA does not guarantee a good observation since its *obscov* may be lower than its neighbours. These patterns of pixel vicinity are displayed on figure 3 for a 200 × 200 pixel zone near the study area.

[Figure 1 about here.]

[Figure 2 about here.]

[Figure 3 about here.]

3. Methodology

The necessary processing steps to prepare comparable GAI products from SPOT and MODIS imagery are henceforth described. The general flowchart in figure 4 may guide the reader throughout the following descriptions.

[Figure 4 about here.]

3.1. Creating a crop specific mask

First and foremost, it is necessary to identify the target objects in the scene. This resumes to having a mask covering the area where the target crop, winter wheat, is to be found in the 2001 growing season. This information could come from various sources other than remote sensing: one could imagine an online vector database of the fields which would be updated by farmers after sowing. However, in this case the only possibility was to classify a set of high spatial resolution images available in the ADAM database. Since this is not the main concern of this study, the methodology used to create this crop mask is only briefly described below.

Five SPOT4 images that are well-distributed along the season were selected from the ADAM database to provide the necessary information to capture winter wheat phenology and discriminate it from other crops across the landscape. NDVI and NDWI are calculated for each image and grouped together in a synthetic 10-band image. This image is then segmented using the multiresolution segmentation algorithm (Baatz & Schäpe, 2000) implemented in Definiens Developer 7 software (Definiens, 2008). The resulting segments, or objects, group spatially-adjacent pixels which have similar trajectories for both vegetation indices over the 5 selected dates. Such multi-temporal segmentation techniques have been used successfully to isolate spatial entities exhibiting change (e.g. Desclée et al., 2006; Duveiller et al., 2008; Bontemps et al., 2008). The segments

are then clustered into groups using an unsupervised classification technique (ISODATA), and these groups are then labelled manually based on visual interpretation and expert knowledge of the landscape.

3.2. Neural network GAI retrieval

In this paper, GAI is retrieved from multispectral reflectance using neural network techniques (NNT) trained over canopy radiative transfer simulations. This hybrid approach combines advantages of statistical and physical approaches in biophysical variable retrieval (Dorigo et al., 2007; Baret & Buis, 2008). The approach is based on the algorithm conceived by Baret et al. (2007) to derive the global LAI product developed within the CYCLOPES (Carbon cYcle and Change in Land Observational Products from an Ensemble of Satellites) project from SPOT/VEGETATION data. The radiative transfer model used is PROSAIL (Baret et al., 1992), a coupling of the canopy reflectance model SAIL (Verhoef, 1984) to the leaf optical properties model PROSPECT (Jacquemoud & Baret, 1990). The CYCLOPES algorithm was later adapted for winter wheat GAI retrieval from the SPOT/HRV(IR) imagery in the ADAM database by Duveiller et al. (2011). This adaptation consisted in: (i) changing the number of neurons with respect to the change in different input bands; (ii) using the appropriate spectral response curves for the HRV and HRVIR instruments; and (iii) using a characterisation of the soil background reflectance specific to Fundulea[4]. The same method was used here to derive GAI maps from SPOT imagery and the method was also adapted to retrieve GAI from MODIS reflectance in the red and near-infrared domains. Back-propagation neural networks with two hidden layers of respectively 5 and 1 neurons are employed. The required input values are VZA, SZA, RAA and the top of canopy reflectance in the different bands. Further description on the construction, training and performance of

[4]Note that the change from LAI in CYCLOPES to GAI in Duveiller et al. (2011) is just a question of terminology since the green elements modelled in PROSAIL can be considered to be approximations of either leaves, stems of ears as long as these are green

the neural networks can be found in Duveiller et al. (2011).

3.3. Modelling the spatial response of MODIS

Since the aim is to compare GAI retrieved from instruments with different spatial resolution, it is necessary to ensure that the observation footprints of both products coincide. Given the large difference in scale between the SPOT and MODIS support, the observation footprint of SPOT can be assumed to be equivalent to the square projection of the pixel. However, due to the complex acquisition system of MODIS, the spatial response of the coarse instrument cannot be neglected.

Having a measure of the spatial response of an instrument in orbit is not easy. Although it is measured in a laboratory under controlled conditions before launching the orbiting platform, there is the possibility for change in a system's PSF after launch due to thermal focus change or instrument outgassing in the space environment (Schowengerdt, 2007). Some techniques can be used to measure the on-board PSF based on specific ground targets in the imagery ((*e.g.* Ruiz & Lopez, 2002)). However, for instruments such as MODIS, the spatial resolution is often too coarse to find appropriate targets and synchronized high spatial resolution imagery might be required (*e.g.* Rojas et al., 2002). MODIS is equipped with a Spectro-radiometric Calibration Assembly (SRCA) (Xiong & Barnes, 2006), which can measure and monitor the actual on-orbit modulation transfer function (MTF)[5]. Nevertheless, this measurement does not take into account the spatial response distortions caused by atmospheric effects. The impact of the spatial response on the imagery available to the user is further distorted pre-processing steps such as resampling.

Given the above-mentioned difficulties in measuring the spatial response, a general but conservative model is built for this study. The net instrument PSF can be modelled by taking into account its different components: the elec-

[5]The MTF is the counterpart of the PSF in the spatial frequency domain and characterizes the attenuation of the spatial frequencies by the imaging instrument

tronic PSF, the detector PSF, the image motion PSF and the optical PSF (Schowengerdt, 2007). For the sake of simplicity the electronic components is neglected. The detector is modelled by a uniform square pulse function:

$$PSF_{det}(x,y) = rect(x/\nu) \cdot rect(y/\nu) \tag{1}$$

where x and y are the spatial coordinates with their origin at the centroid of the ground-projection of the detector's instantaneous field of view, ν is the detector width and $rect(x/\nu)$ is the rectangular function (which is a square pulse of amplitude one and width ν). While the along-track image motion can be disregarded for MODIS, the across-track must be taken into account since the integration time corresponding to image motion as the rotating mirror scans the Earth is nearly a whole detector width (Schowengerdt, 2007). The detector and image motion PSFs can be combined into a scan PSF:

$$PSF_{scan}(x,y) = PSF_{det}(x,y) * PSF_{IM}(x,y) \tag{2}$$

This scan PSF is modelled as a triangular PSF in the across-track direction[6] and as a rectangular PSF in the along-track direction. PSF_{scan} must therefore be inclined according to the angle, j, between the ground track of the satellite and the north–south direction. This angle varies with the latitude, φ, according to Capderou (2005):

$$j = \arctan\left[\frac{\cos i - (1/\kappa)\cos^2\varphi}{\sqrt{\cos^2\phi - \cos^2 i}}\right] \tag{3}$$

where κ is the satellite's daily recurrence frequency and i is the inclination angle (*i.e.* the angle between the orbital plane and the equatorial plane). Finally, the optical component is assumed to have a Gaussian behaviour

$$PSF_{opt}(x,y) = \exp\left(-\frac{x^2+y^2}{2(\nu\sigma)^2}\right) \tag{4}$$

where σ is the standard deviation of the Gaussian curve. In this case $\nu\sigma$ was set to the plausible value of 50 m. The net PSF is a convolution of the scan

[6]Which is the along-scan direction for MODIS since it is a whisk-broom instrument.

PSF obtained in equation 2 with the optical PSF of equation 4 as illustrated in figure 5 and resumed by the following equation:

$$PSF_{net}(x,y) = PSF_{scan}(x,y) * PSF_{opt}(x,y) \quad (5)$$

PSF_{net} is also depicted in 3 dimensions in figure 6. The corresponding MTF model was compared to the on-board MTF measurements provided MODIS Characterization Support Team. The result, shown in figure 7, indicate that the model provides a reasonable approximation. Furthermore it confirms that the value of 50 m for σ in PSF_{opt} is plausible since the modelled spatial response (the solid line) is close to the validation measurements (the crosses).

[Figure 5 about here.]

[Figure 6 about here.]

[Figure 7 about here.]

3.4. Convolution of the spatial response over the SPOT imagery

The next step to make the observation footprints of SPOT and MODIS coincide is to convolve the MODIS spatial response model over the SPOT products (the crop mask and the GAI maps). To do so, the PSF_{net} is discretized to 20 m: the spatial resolution of the SPOT images. The change in support is then realized by applying a bi-dimensional convolution of the spatial response model over the target image Img:

$$\Pi_{Img}(x,y) = Img(x,y) * PSF_{net}(x,y). \quad (6)$$

Every pixel of the resulting image $\Pi_{Img}(x,y)$ displays the value corresponding to a MODIS observation whose centroid falls at that (x,y) coordinate. When applied to the crop specific mask, the result is what will henceforth be referred to as a crop specific pixel purity map. This map indicates the purity of MODIS observations with respect to our target crop: winter wheat. When the convolution is applied to the GAI maps, the resulting convolved maps indicate the GAI

that can be expected when estimated with a MODIS observation support. It must be acknowledged that this does not take into account the gridding effect that may occur when the MODIS observation is stored in the L2G grid.

3.5. Producing adequate MODIS time series

The last step consists in building GAI time series for an ensemble of points were MODIS crop specific pixel purity is above a certain threshold. Two types of time series are to be produced: (i) simulated MODIS GAI time series obtained from the convolved GAI maps produced from SPOT imagery (TS_{sim}); and (ii) actual MODIS GAI time series obtained by retrieved GAI from MODIS reflectances (TS_{obs}). While the latter contain GAI estimations obtained with variable observation geometry (*i.e.* VZA and *obscov*), the former are simulations of GAI obtained from MODIS in ideal conditions: that is at nadir and without gridding artifacts.

To identify the desired pixels in the L2G grid that must be used, the geolocation of their centroids in the MODIS sinusoidal projection is retained. These values are re-projected into the Gauss-Kruger projection in which the SPOT products within the ADAM database are projected. For each point, the corresponding MODIS purity is extracted from the crop specific pixel purity map. It must be acknowledged that this procedure for associating the purity to a cell in the L2G grid is an approximation because gridding artifacts are neglected (normally the centroid of the observation footprint is not going to be the same as the grid cell centroid). Pixel purity must therefore be taken as an indicator of the amount of interesting information present in the cell rather than an absolute measurement.

Since the main interest of this paper is time series dominated by wheat, only MODIS grid cells with at least 75% of purity are kept for the analyses. For these pure enough grid cells and for all available dates, the MODIS reflectances are transformed into GAI using a MODIS specific NNT to produce TS_{obs}. This set of time series also contains information on VZA and *obscov* for every individual MODIS acquisitions. To produce the other set of time series, TS_{sim}, GAI is

simply extracted from the convolved GAI maps for all selected grid cells in the same way as purity was obtained from the crop specific pixel purity maps.

3.6. Temporal smoothing

The SPOT high spatial resolution imagery do not necessarily coincide in time with the MODIS observations. In order to compare the GAI derived from both instruments, a canopy structural dynamic model (CSDM) can be used to smooth out one of the GAI estimation time series. The CSDM is a simple semi-mechanistic model which describes the combined effect of growth and senescence with respect to thermal time by means of a mathematical expression. The CSDM both smooths the residual errors associated to each individual GAI estimation and describes continuously the biophysical variable's time course from a limited number of observations during the growth cycle (Koetz et al., 2005). In this study, a CSDM developed by Baret (1986) and improved by Lauvernet (2005) is used, with the only difference that the biophysical variable is here labelled GAI instead of LAI. The mathematical expression is the following:

$$GAI(tt) = k \cdot \left[\frac{1}{(1 + e^{-a(tt - T_0 - T_a)})^c} - e^{b(tt - T_0 - T_b)} \right] \quad (7)$$

where a and b define the rates of growth and senescence, c is a parameter allowing some plasticity to the shape of the curve, k is a scaling coefficient and T_0, T_a and T_b are the thermal times of plant emergence, mid-growth and end of senescence. The CSDM is further parametrized so as to yield zero GAI once senescence is finished.

The driving variable of the CSDM is thermal time (tt) or cumulated growing degree-days. The thermal time for a single day tt_i is calculated in the following way:

$$tt_i = \left[\frac{(T_{max} + T_{min})}{2} \right] - T_{base} \quad (8)$$

based on the daily minimum (T_{min}) and maximum (T_{max}) air temperatures recorded at the Fundulea meteo station. T_{base} is the temperature below which the process of interest, in this case winter wheat growth, does not progress. The

base temperature used here for winter wheat is 0°C and the starting date for the temperature sum is October 1st, 2000, which corresponds to the sowing period.

3.7. Statistical indicators

The following analyses will also require to quantify the correspondence between GAI products. The discrepancies between a given product and a reference product will be compared using the statistical indicators presented in table 2. Amongst these, B and S are two subcomponents of the total discrepancy quantified by the $RMSE$ and are related by the formula: $RMSE^2 = B^2 + S^2$.

[Table 2 about here.]

4. Results

The analysis of the data generated in this study is focused on answering three questions concerning GAI estimation from both fine and coarse spatial resolution.

4.1. How does pixel purity influence GAI regional estimation?

This question can be reasoned by analysing the bias that may occur between the median GAI obtained over all wheat fields in the region from fine spatial resolution and the median GAI obtained from coarse spatial resolution GAI estimations. This bias, δ, is expected to occur because wheat GAI estimations from coarse spatial resolution can be contaminated by the signal from non-wheat surfaces located within the observation footprint. Therefore, δ depends on the crop specific pixel purity threshold (π) used to select a the population of coarse spatial resolution GAI estimates that will represent the regional estimation.

To analyse how δ varies with π along the growing season, only the convolved and original GAI maps derived from SPOT are used. For every date in which there is a SPOT image, the median GAI of the region is calculated using all wheat pixels in the corresponding original GAI map. δ is then calculated for

increasing values of π by subtracting the median GAI obtained from pixel population of the convolved maps selected using the given threshold π. Figure 8 describes the evolution of δ with respect to π for the various dates at which GAI maps are available (the curves in figure 8 are actually 4th order polynomials fitted on punctual δ values obtained with 100 discrete π values from 1 to 100).

[Figure 8 about here.]

Figure 8 clearly shows how the π values used to select GAI estimations from the convolved maps have an effect on how well these estimations represent the median regional GAI obtained from the original GAI maps. Both the magnitude and the direction of this effect varies along the growing season. Early in the season (dark curves on figure 8) the bias is practically close to zero for all values of π because GAI values are low overall and there is little difference between the target (winter wheat) and non-target surfaces (mostly other crops). Later in the season, the winter wheat has higher GAI than neighbouring surfaces and thus, selections of "purer" pixels (higher π) are necessary to limit the contamination effect from non-wheat surfaces which would bring down the median GAI estimation (thereby increasing δ). Late in the season (light curves on figure 8), summer crops surrounding the target winter wheat fields have a higher GAI, and therefore δ takes negative values when π is low and contamination occurs. Overall there is a convergence towards $\delta = 0$ when purity thresholds increase: a high π threshold will generally result in a smaller $|\delta|$ by favouring observations which are more dominated with the target crop[7]. This illustrates the importance of pixel purity on the regional GAI estimation. The convergence of the curves in figure 8 also indicates that the GAI retrieval algorithm is not really scale dependent for the considered spatial resolutions.

[7]Note, however, that if π is too restrictive and the reduction of selected pixels is too severe, the pixel selection might not be representative of the median GAI across the study area any more, thereby causing an increase in $|\delta|$

The minimum pixel purity requirements to study the landscape can be defined by fixing a $|\delta|$ which can be considered as acceptable. To illustrate how this minimum acceptable pixel purity is temporally dependent along the winter wheat growing season, the π values at which the curves in figure 8 reach $|\delta| = 0.10$ and $|\delta| = 0.05$ are displayed on the top panel of figure 9. Since it is inconvenient to change the pixel purity thresholds along the season (because this creates gaps in the time series), it is more practical to know the potential bias that can occur with a fixed pixel purity threshold and how this bias evolves along the season. This is illustrated on the bottom panel of figure 9 for different π thresholds.

[Figure 9 about here.]

4.2. Can MODIS acquisition information be used to improve GAI estimation?

The GAI upscaled from SPOT to MODIS resolution, TS_{sim}, is considered to be at nadir and does not suffer from *obscov* local variations. However, the real MODIS data are rarely at nadir and have variable *obscov*. To exploit all MODIS observations it is necessary to analyse the effect of these two variables on the quality of the GAI estimation. This is done by comparing the two ensemble of time series: TS_{sim} and TS_{obs}. In order to analyse all MODIS observations within TS_{obs}, these are compared to $\hat{TS_{sim}}$, the temporal interpolation of TS_{sim} using the CSDM (Eq. 7). The effect of VZA and *obscov* thresholds is then analysed. For increasing thresholds of *obscov* and decreasing thresholds of VZA, selections of fewer, but presumably more reliable estimations are made. For each selection of points, statistical indicators are calculated by considering that $\hat{TS_{sim}}$ is the reference time series (z in equations in table 2) and TS_{obs} is the estimation ($\hat{z}$ in equations in table 2). The result can be visualized in iso-contour plots to see the combined effect of thresholds on both VZA and *obscov* (see figure 10). These graphs reveal an interesting point: desirable points do not need to satisfy simultaneously the conditions for the two variables. In other words, if an observation has a favourable *obscov*, it can

have an unfavourable VZA (and vice versa) and still remain reliable. To illustrate the potential improvement that can be achieved by taking into account *obscov* and VZA, the dataset Z, consisting of all individual GAI estimations in TS_{obs}, is stratified into different groups for which the concurrent TS_{obs} and $\hat{TS}_{sim}$ are compared. The groups are based on a single threshold for each variable, defined so that if taken by itself, at least 30% of the points remain. This yields a maximum acceptable VZA of 24° and a minumum acceptable *obscov* of 0.36. Figure 11 shows how both individual thresholds significantly filter out sub-optimal estimations, and how combining them by retaining the union of both constraints ($z_1 \subset Z : VZA \leq 24° \cup obscov \geq 0.36$) rather than their intersection ($z_2 \subset Z : VZA \leq 24° \cap obscov \geq 0.36$), the amount of usable points increases by 20% of the total amount Z.

[Figure 10 about here.]

[Figure 11 about here.]

The thresholding on *obscov* and VZA is expected to improve the temporal consistency of MODIS estimates. To test this, the CSDM is fitted for all available time series using all available points (*i.e.* without any restrictions on either VZA or *obscov*). This temporally-smoothed GAI estimation is used as a reference, to which different sets of punctual GAI estimations are compared. The results in table 3 confirm that filtering[8] MODIS estimations by either satisfying a *obscov* or a VZA criteria improves the temporal consistency as shown by the reduction of RRMSE. This is not merely an effect of sample number reduction as when a random sample set of equal size is used (the group labelled z_3 in table reftab:TempCons), the statistical indicators remain comparable to when all points are used. Furthermore, the comparison between z_1 (union) and z_2 (intersection) shows that although the temporal consistency is slightly improved

[8]The term filtering, i.e. removing unwanted observation, must not be confused with the smoothing operation done with the CSDM in which the objective is removing the errors on the observations.

for z_2, it comes at the expense of a serious reduction of observations per time series.

[Table 3 about here.]

The bias of all cases in table 3 is slightly negative. The reason is that the fitting of a CSDM will always bring values around the peak down. Subset z_1 actually shows a more negative bias. This value can be reduced by fitting a CSDM on these values only. This indicates that by filtering out bad values, the overall GAI estimates are lower.

4.3. How do MODIS GAI estimations compare to high spatial resolution GAI?

The last question that must be addressed is how well do the MODIS GAI estimations in TS_{obs} relate to the original (non-convolved) GAI maps, and whether they can characterize the regional GAI variability and its temporal dynamic. Hereafter, only the temporally smoothed profile based on $VZA \leq 24° \cup obscov \geq 0.36$ are used on the MODIS side. These are first compared to the punctual SPOT upscaled GAI estimations and the resulting statistical indicators are displayed in figure 12. As expected, the performance is related to the date of acquisition: GAI is harder to estimate when it reaches its peak value (*i.e.* on DoY 123). However, the bias between MODIS and SPOT fluctuates along the season revealing shortcomings of the GAI SPOT estimation with respect to the MODIS smoothed estimation. These might be explained by errors in SPOT radiometric pre-processing but also by an inadequacy of the retrieval algorithm to correctly take into account the differences in acquisition geometry in the SPOT time series[9]. This bias effect penalizes the performance indicated by the RMSE, and even more so for the relative RMSE (*e.g.* DoY = 76). However, the dispersion of the estimation characterized by CV remains relatively stable all along the season suggesting that the overall performance of the MODIS GAI is stable.

[9]Note that this kind of errors are also expected from the MODIS side but these are smoothed out in this case by the CSDM.

[Figure 12 about here.]

Pixel purity affects the performance as well. Figure 13 shows how the RMSE, its constitutive parts (B and S) and the coefficient of variation (CV) vary for increasing pixel purity thresholds. As purity increases, the bias generally becomes more positive while the dispersion decreases. The reduction of S is easily understandable given the reduction of surface heterogeneity that pixel purity assures. The change in B results from the fact that SPOT convoluted estimations have the footprint of an ideal at-nadir simulation without gridding artefacts while the footprint of the MODIS estimations is affected by *obscov* and VZA, and is therefore potentially more contaminated with non-wheat GAI when π is low. For the same reasons as mentioned in section 4.1, more contamination (*i.e.* less purity) will result in lower GAI during the main growing season when wheat GAI is higher than the GAI of neighbouring surfaces.

[Figure 13 about here.]

The main objective of using MODIS is to provide crop specific GAI information at a regional level, *i.e.* the 40 × 40 km study area. To do so, the ensemble TS_{obs} over the study area will be compared to the distribution of all points in the fine spatial resolution GAI map falling within the winter wheat mask. As it has been mentioned above, there is bias between MODIS and SPOT GAI estimations which is variable according the time of acquisition of the SPOT imagery. Since the objective here is to assess the performance of the GAI obtained from MODIS, and not from SPOT, the bias for each SPOT GAI map compared to the concurrent MODIS estimation is removed from the entire map prior to estimating the regional range of GAI. Figure 14 summarizes the comparison at regional level by showing the boxplots of the SPOT GAI distributions overlayed over the ensemble of MODIS time series above 85% of crop specific purity before and after the bias correction. A visual assessment of the spatial correlation between the MODIS punctual GAI estimations and the corrected SPOT GAI maps is presented in figure 15. It reveals that the MODIS estimations not only

grasp the inter-field variability reasonably well, but they can also characterize more subtle intra-field spatial differences over the larger fields.

[Figure 14 about here.]

[Figure 15 about here.]

To further evaluate how representative the MODIS estimations are with respect to the regional behaviour of all fields, the bias correction between SPOT and MODIS is done based on pixels selected with various increasing π thresholds. Table 4 resumes the RMSE for the estimation of different percentiles of the regional GAI with different levels of purity. The RMSE between both estimations of the median values is better for 85% purity than 95% suggesting that an overly harsh purity threshold might not be desirable to characterize the general GAI dynamic.

[Table 4 about here.]

5. Discussion

The results demonstrate that, by controlling pixel-target adequacy, it is possible to characterize both the spatial range and temporal dynamics of crop specific GAI at a regional scale with coarse spatial resolution imagery. The difference in performance between MODIS and fine spatial resolution to estimate the median GAI over the 40 $\times$ 40 km study region can be reduced to an RMSE of 0.053 m^2/m^2 by filtering in the spatial and temporal dimensions using appropriate thresholds on pixel purity, *obscov* and VZA. These results confirm the robustness of the retrieval algorithm after training it over learning databases with the same radiative transfer parametrisation but applying it to different instruments. Furthermore, the MODIS GAI estimations are generally coherent with fine spatial resolution GAI maps at both inter-field and intra-field levels.

The proposed approach can be generalized to other medium spatial resolution instruments. Demonstrating the methodology on MODIS was a choice to

reach a large spectrum of potential users since MODIS data are widely used due to its easy availability and free access for the Earth observation community. However, MODIS was also chosen to demonstrate the applicability of the methods to data acquired with a complex acquisition geometry (whiskbroom configuration, wide scan angle, triangular PSF). It must be recognized that the target-support adequacy problems addressed in this paper are largely due to the artefacts brought by the gridding of MODIS observations in a raster grid (Tan et al., 2006; Kristof & Pataki, 2009). VZA and *obscov* are used as proxies of the adequacy between observation support and target. An alternative to avoid this problem has been proposed by (Kristof & Pataki, 2009) in which they re-process the raw MODIS data and instead of assigning the reflectance value to a raster grid cell, they assign it to vectors describing the observation footprints. Although this approach is bound to provide reflectance of higher quality, it is much more complex and computationally expensive, hindering its operational use. Our approach has the advantage of being applicable to standard "off-the-shelf" pre-processed MODIS products which are widely used in the scientific community. The approach proposed here could also be applied to MERIS since it has been shown that pushbroom instruments also have gridding artifacts which should be taken into account when looking at multi-temporal pixel entities (Gomez-Chova et al., 2011). Concerning the relevance of deploying such effort to control the spatial response of instruments which are nearing the end of their expected lifetime, it can be argued that both MODIS and MERIS will retain a significant importance as a long term record. Furthermore, the operational successor of MODIS instruments, the VIIRS instrument which will be onboard of the NPOESS satellite, will have a similar whiskbroom configuration and slightly coarser spatial resolution (Miller et al., 2006).

This experiment reveals that there is a bias between MODIS and SPOT GAI estimations that varies along the season, potentially indicating errors in the GAI derivation that may come from less accurate radiometric measurements of SPOT radiances as well as from the atmospheric correction or from the neural network biophysical algorithm. In this study, it was chosen to correct this bias based

on the temporal consistency of the GAI dynamic estimated by the instrument providing the highest observation repetitivity: MODIS. This is a fine illustration of instrument complementarity whereby the high temporal resolution of Terra/MODIS assures the general trajectory and the high spatial resolution of SPOT/HRV(IR) could be used to estimate the local spatial heterogeneity of GAI. Such benefits of joint exploitation of data should be considered in designing future Earth observation missions. In this regards, much can be expected from the combination of the global coverage at 20 m every 5 days using Sentinel-2 platforms with the daily global coverage at 300 m of Sentinel-3. Before that, a better opportunity to combine high temporal repetitivity with high spatial resolution will come with the programmed PROBA-V satellite whose cameras allow the adquistion of data with 100 m spatial resolution approximately every 5 days and daily data at 300 m. Before these future missions become operational, GAI could be derived from wide swath imagery with high spatial resolution such as AWiFS or DMC using a similar neural network approach, and such GAI estimation could be used to asses the sub-pixel spatial heterogeneity of coarse spatial resolution GAI over large geographic coverages. A pre-requisite is to have an information on the spectral response of these instruments which unfortunately is not always simple to obtain.

Before extending the approach described here to other agricultural sites, it is necessary to consider some technical issues. For instance, the selection of thresholds for pixel purity, VZA and *obscov* limits the number of available GAI estimations and ultimately impacts the accuracy of the overall result. It has been shown that a judicious thresholds on VZA and *obscov* improves the temporal consistency of the estimations (section 4.2) while spatial filtering based on pixel purity is necessary to avoid affecting the regional GAI characterization (section 4.1). However, the threshold values proposed here should not necessarily be transposed to other study sites. The value of VZA and *obscov* as proxies of target-observation adequacy will vary with landscape fragmentation and crop rotation. Instead threshold choices should be reasoned with respect to data availability (which is dependent on cloud coverage). In this respect, it has

been shown that using both VZA and *obscov* in a non-exclusive way enables to conserve more GAI estimations than combined exclusive thresholds without compromising the accuracy. Perhaps further improvements could be achieved by assigning non-binary weights depending on favourable VZA and *obscov* values instead of thresholding. However, the problem is then to choose the values for these weights. Concerning the choice of pixel purity thresholds, the analysis in section 4.1 provides insight into how it has to be reasoned according to time window of interest. The values obtained for maximum tolerable thresholds are to be considered in relative terms, as their absolute values will vary according to the choice of the statistical test used, its parametrization and the sub-sampling protocol that is employed. The temporal variation of this pixel purity threshold may be explained based on the variability of temporal GAI trajectories within the crop-specific mask, explaining the necessity of higher purity thresholds around the mid-season when winter wheat fields are less synchronised between each other. Later in the season, winter wheat fields are all back to low GAI, but surrounding summer crops have higher GAI which will contaminate GAI estimations unless high pixel purity values are selected. Since it would not be practical to change the threshold along the season, it seems appropriate to choose one assuring a good performance over most of the time window of interest, *i.e.* the window which would be more suitable for assimilating GAI into crop growth models. An upper limit for purity threshold could also be necessary if sampling within the larger fields biases the regional GAI estimation. In some landscapes such bias has been shown not to be present (*e.g.* Guissard et al., 2004). Over the study site, the analysis in section 4.1 does not detect that higher purity thresholds such as 95% provide biased estimations of the regional GAI. However, the results in table 4 do indicate that an overly harsh purity threshold is less appropriate to correctly characterize the regional distribution.

The crop mask at fine spatial resolution is necessary to assure regional crop specific GAI estimation with MODIS. Constructing this mask will require fine spatial resolution imagery, which is precisely one of the drawbacks of the other methods to deal with heterogeneous surfaces: downscaling (Zurita-Milla et al.,

2009) and correcting the scaling bias (Garrigues et al., 2006a, 2008). However, to build a crop mask, imagery acquired at any time during the growing season will be useful whereas for the other approaches, the imagery should preferably fall when it GAI estimations are more critical, *i.e.* during the fast growing phase which often coincides with smaller acquisition success due to increased cloud cover. Another issue concerning the crop mask is that, throughout this study, it has been implicitly assumed that for the target crop intra-field and inter-field heterogeneity is much smaller than the heterogeneity between the target crop and other land cover types. In some agricultural landscapes, the differences might not be so important because there is much GAI variability within a same field, or because the crop is confounded with neighbouring vegetation. In such a case, the notion of crop specific pixel purity might have to be revisited, perhaps using a fuzzy mask instead of a crisp binary mask to characterize the landscape.

The methodology presented here also calls for a relatively detailed model of the spatial response of MODIS in order to calculate pixel purity. Is is necessary to take the PSF into account or could a simple aggregation of the crop mask to a 250 m square pixel could be enough? This latter option is equivalent to modelling only the detector PSF with a square-wave function. Studies have shown that this simplified approach has an impact on land cover characterization that can be controlled by using a finer estimation of the instrument's spatial response (Townshend et al., 2000; Huang et al., 2002). When seeking the coarsest acceptable spatial resolution requirements for agricultural monitoring, Duveiller & Defourny (2010) found that these are systematically over-estimated when using a square PSF instead of a model composed of both optical and detector components of the instrument's spatial response. Of course, the impact of modelling correctly the PSF on pixel purity is particularly important when the size of the observed objects are close to the size of the observation footprint.

A final point of discussion needs to address the smoothing of GAI with the CSDM. It must be acknowledged that relating GAI growth and senescence exclusively to thermal time is a simplification since this dynamic can be strongly influenced by other factors such as nitrogen deficiency and pest attacks. How-

ever, it is very difficult to have enough *a priori* information on these other factors to take them into account over a large geographic extent using a more sophisticated crop growth model for instance. Taking a time frame based on temperature, one of the main drivers of plant physiological processes, is already a significant improvement compared to just measuring time in days which are much less relevant for the crops.

6. Conclusion

By taking winter wheat as an example, this paper demonstrates that crop specific GAI estimations retrieved from coarse spatial resolution imagery such as MODIS are adequate to characterize crop dynamics at a regional scale. To achieve this, it is necessary to control the degree at which the observation footprints of the coarse pixels fall within the crop-specific mask delineating the target. This control is done by filtering out less reliable GAI estimations in both the spatial and temporal dimensions using thresholds on pixel purity, *obscov* and VZA which were determined for this study.

The experiment has also demonstrated the possibility to retrieve coherent GAI estimates from different data with different scales using the same technique involving radiative transfer modelling and neural networks. Some shortcomings of the retrieval do exist, as revealed by the variable bias between high and coarse spatial resolution estimates at the different studied dates. However, these deviations can be corrected in a fine example of instrument complementarity whereby the high temporal resolution assures the general GAI trajectory and the high spatial resolution can be used to estimate the local spatial heterogeneity.

The concern of assuring pixel-target adequacy, widely addressed in this paper, is not limited to GAI nor agricultural monitoring. The proposed approach could indeed be used for any other application in which the output can be based on a subset of pixel samples within the scene. Although technological improvements are bound to provide finer spatial resolution data with more frequent revisit times, pixel-target adequacy will remain important for various remote

sensing application because once the technology arrives, users will naturally be inclined to look closer, more frequently and with more detail.

Acknowledgment

This research was funded by the Belgian *Fond de la Recherche Scientifique – FNRS* by way of a PhD grant to the first author. The research also falls in the framework of the GLOBAM project which is financed by the Belgian Scientific Policy (BELSPO) with the STEREO II programme. The data used in this paper are part of the ADAM database made available by Kalideos (http://kalideos.cnes.fr) and the SPOT imagery have the following copyright: CNES 2001 - Distribution Spot Image. The authors would like to thank Jim Tucker, Jean-Francois Ledent, Patrick Bogaert and the four anonymous reviewers for their comments and suggestions which have contributed to improve significantly this document. The authors also thank the MODIS Characterization Support Team (MCST) for providing specific details of the MODIS PSF.

Baatz, M. & Schäpe, A. (2000). Multiresolution Segmentation - an optimization approach for high quality multi-scale image segmentation, in Strobl, J., Blaschke, T., & Griesebner, G., eds., *Angewandte Geographische Informationsverarbeitung XII*, (pp. 12–23), Wichmann-Verlag, Heidelberg

Baret, F. (1986). *Contribution au suivi radiométrique de cultures de céréales*, Ph.D. thesis, Université de Paris-Sud

Baret, F. & Buis, S. (2008). *Advances in Land Remote Sensing. System, Modeling, Inversion and Application*, chap. Estimating canopy characteristics from remote sensing observations. Review of methods and associated problems, (pp. 173–201), Springer Netherlands

Baret, F., Hagolle, O., Geiger, B., Bicheron, P., Miras, B., Huc, M., Berthelot, B., Nino, F., Weiss, M., Samain, O., Roujean, J. L., & Leroy, M. (2007).

LAI, fAPAR and fCover CYCLOPES global products derived from VEGETATION: Part 1: Principles of the algorithm, *Remote Sensing of Environment*, *110* (3), 275–286

Baret, F., Jacquemoud, S., Guyot, G., & Leprieur, C. (1992). Modeled Analysis of the Biophysical Nature of Spectral Shifts and Comparison With Information-content of Broad Bands, *Remote Sensing of Environment*, *41* (2-3), 133–142

Baret, F., Vintila, R., Lazar, C., Rochdi, N., Prevot, L., Favard, J. C., Boissezon, H. d., Lauvernet, C., Petcu, E., Petcu, G., Voicu, P., Denux, J. P., Poenaru, V., Marloie, O., Simota, C., Radnea, C., Turnea, D., Cabot, F., & Henry, P. (2001). The ADAM database and its potential to investigate high temporal sampling acquisition at high spatial resolution for the monitoring of agricultural crops., *Romanian Agricultural Research*, (No.16), 69–80

Bontemps, S., Bogaert, P., Titeux, N., & Defourny, P. (2008). An object-based change detection method accounting for temporal dependences in time series with medium to coarse spatial resolution, *Remote Sensing of Environment*, *112* (6), 3181–3191

Brisson, N., Mary, B., Ripoche, D., Jeuffroy, M. H., Ruget, F., Nicoullaud, B., Gate, P., Devienne-Barret, F., Antonioletti, R., Durr, C., Richard, G., Beaudoin, N., Recous, S., Tayot, X., Plenet, D., Cellier, P., Machet, J.-M., Meynard, J. M., & Delécolle, R. (1998). STICS: a generic model for the simulation of crops and their water and nitrogen balances. I. Theory and parameterization applied to wheat and corn, *Agronomie*, *18* (5-6), 311–346

Capderou, M. (2005). *Satellites Orbits and Missions*, Springer Paris

Cayrol, P., Kergoat, L., Moulin, S., Dedieu, G., & Chehbouni, A. (2000). Calibrating a Coupled SVAT-Vegetation Growth Model with Remotely Sensed Reflectance and Surface Temperature – A Case Study for the HAPEX-Sahel Grassland Sites, *Journal of Applied Meteorology*, *39* (12), 2452–2472

Chen, J. M. & Black, T. A. (1992). Defining leaf area index for non-flat leaves, *Plant, Cell and Environment*, *15* (4), 421–429

Cracknell, A. (1998). Synergy in remote sensing–What's in a pixel?, *International Journal of Remote Sensing*, *19* (11), 2025–2047

Definiens (2008). *Definiens Developer 7 User Guide*, Definiens, Definiens AG Trappentreustr. 1 D-80339 München Germany, document version 7.0.5.968 edn.

Deng, F., Chen, J., Plummer, S., Chen, M., & Pisek, J. (2006). Algorithm for Global Leaf Area Index Retrieval Using Satellite Imagery, *Geoscience and Remote Sensing, IEEE Transactions on*, *44* (8), 2219–2229

Desclée, B., Bogaert, P., & Defourny, P. (2006). Forest change detection by statistical object-based method, *Remote Sensing of Environment*, *102* (1-2), 1–11

Dorigo, W., Zurita-Milla, R., de Wit, A., Brazile, J., Singh, R., & Schaepman, M. (2007). A review on reflective remote sensing and data assimilation techniques for enhanced agroecosystem modeling, *International Journal of Applied Earth Observation and Geoinformation*, *9*, 165–193

Duveiller, G. & Defourny, P. (2010). A conceptual framework to define the spatial resolution requirements for agricultural monitoring using remote sensing, *Remote Sensing of Environment*, *114* (11), 2637–2650

Duveiller, G., Defourny, P., Desclée, B., & Mayaux, P. (2008). Deforestation in Central Africa: Estimates at regional, national and landscape levels by advanced processing of systematically-distributed Landsat extracts, *Remote Sensing of Environment*, *112* (5), 1969–1981

Duveiller, G., Weiss, M., Baret, F., & Defourny, P. (2011). Retrieving wheat Green Area Index during the growing season from optical time series measurements based on neural network radiative transfer inversion, *Remote Sensing of Environment*, *115* (3), 887–896

Friedl, M., Davis, F., Michaelsen, J., & Moritz, M. (1995). Scaling and uncertainty in the relationship between the NDVI and land surface biophysical variables: an analysis using a scene simulation model and data from FIFE, *Remote Sensing of Environment*, *54*, 233–246

Garrigues, S., Allard, D., & Baret, F. (2008). Modeling temporal changes in surface spatial heterogeneity over an agricultural site, *Remote Sensing of Environment*, *112* (2), 588–602

Garrigues, S., Allard, D., Baret, F., & Weiss, M. (2006a). Influence of landscape spatial heterogeneity on the non-linear estimation of leaf area index from moderate spatial resolution remote sensing data, *Remote Sensing of Environment*, *105* (4), 286–298

Garrigues, S., Allard, D., Baret, F., & Weiss, M. (2006b). Quantifying spatial heterogeneity at the landscape scale using variogram models, *Remote Sensing of Environment*, *103* (1), 81–96

Genovese, G., Vignolles, C., Nègre, T., & Passera, G. (2001). A methodology for a combined use of normalised difference vegetation index and CORINE land cover data for crop yield monitoring and forecasting. A case study on Spain, *Agronomie*, *21*, 91–111

Gomez-Chova, L., Zurita-Milla, R., Alonso, L., Amoros-Lopez, J., Guanter, L., & Camps-Valls, G. (2011). Gridding Artifacts on Medium-Resolution Satellite Image Time Series: MERIS Case Study, *Geoscience and Remote Sensing, IEEE Transactions on*, *PP* (99), 1–11

Guissard, V., Defourny, P., & Ledent, J.-F. (2004). Crop specific information extraction based on coarse resolution pixel sampling, in *2nd VEGETATION Int. User Conf., Antwerp, Belgium, 2004*.

Huang, C., Townshend, J. R. G., Liang, S., Kalluri, S. N. V., & DeFries, R. S. (2002). Impact of sensor's point spread function on land cover characteriza-

tion: assessment and deconvolution, *Remote Sensing of Environment*, *80* (2), 203–212

Jacquemoud, S. & Baret, F. (1990). PROSPECT: A model of leaf optical properties spectra, *Remote Sensing of Environment*, *34* (2), 75–91

Kastens, J. H., Kastens, T. L., Kastens, D. L., Price, K. P., Martinko, E. A., & Lee, R.-Y. (2005). Image masking for crop yield forecasting using AVHRR NDVI time series imagery, *Remote Sensing of Environment*, *99* (3), 341–356

Khlopenkov, K. & Trishchenko, A. (2008). Implementation and Evaluation of Concurrent Gradient Search Method for Reprojection of MODIS Level 1B Imagery, *Geoscience and Remote Sensing, IEEE Transactions on DOI - 10.1109/TGRS.2008.916633*, *46* (7), 2016–2027

Koetz, B., Baret, F., Poilve, H., & Hill, J. (2005). Use of coupled canopy structure dynamic and radiative transfer models to estimate biophysical canopy characteristics, *Remote Sensing of Environment*, *95* (1), 115–124

Kristof, D. & Pataki, R. (2009). Tackling with the limitations of the raster data model: vector-based preprocessing of modis reflective bands, in Civco, D. L., ed., *Fifth International Workshop on the Analysis of Multi-temporal Remote Sensing Images*, (pp. 160–167)

Lauvernet, C. (2005). *Assimilation variationnelle d'observations de télédétection dans les modèles de fonctionnement de la végétation : utilisation du modèle adjoint et prise en compte de contraintes spatiales.*, Ph.D. thesis, Université Joseph Fourier - Grenoble

Los, S., Pollack, N., Parris, M., Collatz, G., Tucker, C., Sellers, P., Malmstrom, C., DeFries, R., Bounoua, L., & Dazlich, D. (2000). A global 9-yr biophysical land surface dataset from NOAA AVHRR data, *Journal of Hydrometeorology*, *1*, 183–199

Masson, V., Champeaux, J.-L., Chauvin, F., Meriguet, C., & Lacaze, R. (2003). A Global Database of Land Surface Parameters at 1-km Resolution in Meteorological and Climate Models, *Journal of Climate*, *16* (9), 1261–1282

Miller, S. D., Hawkins, J. D., Kent, J., Turk, F. J., Lee, T. F., Kuciauskas, A. P., Richardson, K., Wade, R., & Hoffman, C. (2006). NexSat: Previewing NPOESS/VIIRS Imagery Capabilities, *Bulletin of the American Meteorological Society*, *87* (4), 433–446

Moulin, S., Bondeau, A., & Delecolle, R. (1998). Combining agricultural crop models and satellite observations: from field to regional scales, *International Journal of Remote Sensing*, *19* (6), 1021–1036

Myneni, R. B., Hoffman, S., Knyazikhin, Y., Privette, J. L., Glassy, J., Tian, Y., Wang, Y., Song, X., Zhang, Y., Smith, G. R., Lotsch, A., Friedl, M., Morisette, J. T., Votava, P., Nemani, R. R., & Running, S. W. (2002). Global products of vegetation leaf area and fraction absorbed PAR from year one of MODIS data, *Remote Sensing of Environment*, *83* (1-2), 214–231

Myneni, R. B., Maggion, S., Iaquinta, J., Privette, J. L., Gobron, N., Pinty, B., Kimes, D. S., Verstraete, M. M., & Williams, D. L. (1995). Optical remote sensing of vegetation: Modeling, caveats, and algorithms, *Remote Sensing of Environment*, *51* (1), 169–188

Nieke, J., Frerick, J., Stroede, J., Mavrocordatos, C., & Berruti, B. (2008). Status of the optical payload and processor development of ESA's Sentinel 3 mission, in *Proceedings of the IEEE International Geoscience & Remote Sensing Symposium, Jul. 2008., Boston, Massachusetts, U.S.A.*, vol. 4, (pp. 145–153)

Rahman, H. & Dedieu, G. (1994). SMAC: a simplified method for the atmospheric correction of satellite measurements in the solar spectrum, *International Journal of Remote Sensing*, *15* (1), 123–143

Rast, M., Bezy, J. L., & Bruzzi, S. (1999). The ESA Medium Resolution Imaging Spectrometer MERIS: a review of the instrument and its mission, *International Journal of Remote Sensing*, *20* (9), 1681–1702

Ren, J., Chen, Z., Zhou, Q., & Tang, H. (2008). Regional yield estimation for winter wheat with MODIS-NDVI data in Shandong, China, *International Journal of Applied Earth Observation and Geoinformation*, *10* (4), 403–413

Ritchie, T., J. & Otter, S. (1985). Description and performance of CERES-Wheat: a user-oriented wheat yield model, in *ARS Wheat Yield Project*, (pp. 159–175), Natl. Technol. Info. Serv., Springfield, MI.

Rojas, F., Schowengerdt, R. A., & Biggar, S. F. (2002). Early results on the characterization of the Terra MODIS spatial response, *Remote Sensing of Environment*, *83* (1-2), 50–61

Ruiz, C. & Lopez, F. (2002). Restoring SPOT images using PSF-derived deconvolution filters, *International Journal of Remote Sensing*, *23*, 2379–2391(13)

Salomonson, V., Barnes, W., Maymon, P., Montgomery, H., & Ostrow, H. (1989). MODIS: advanced facility instrument for studies of the Earth as a system, *Geoscience and Remote Sensing, IEEE Transactions on DOI - 10.1109/36.20292*, *27* (2), 145–153

Schowengerdt (2007). *Remote sensing: models and methods for image processing*, San Diego: Academic Press., 3rd edn.

Sellers, P. J., Tucker, C. J., Collatz, G. J., Los, S. O., Justice, C. O., Dazlich, D. A., & Randall, D. A. (1994). A global 1° by 1° NDVI data set for climate studies. Part 2: The generation of global fields of terrestrial biophysical parameters from the NDVI, *International Journal of Remote Sensing*, *15* (17), 3519–3545

Tan, B., Woodcock, C., Hu, J., Zhang, P., Ozdogan, M., Huang, D., Yang, W., Knyazikhin, Y., & Myneni, R. (2006). The impact of gridding artifacts on

the local spatial properties of MODIS data: Implications for validation, compositing, and band-to-band registration across resolutions, *Remote Sensing of Environment*, *105* (2), 98–114

Townshend, J. R. G., Huang, C., Kalluri, S. N. V., Defries, R. S., Liang, S., & Yang, K. (2000). Beware of per-pixel characterization of land cover, *International Journal of Remote Sensing*, *21*, 839–843(5)

van Diepen, C., Wolf, J., van Keulen, H., & Rappoldf, C. (1989). WOFOST: A simulation model of crop production., *Soil Use Management*, *5*, 16–24

Verhoef, W. (1984). Light scattering by leaf layers with application to canopy reflectance modeling: The SAIL model, *Remote Sensing of Environment*, *16* (2), 125–141

Wolfe, R. E., Nishihama, M., Fleig, A. J., Kuyper, J. A., Roy, D. P., Storey, J. C., & Patt, F. S. (2002). Achieving sub-pixel geolocation accuracy in support of MODIS land science, *Remote Sensing of Environment*, *83* (1-2), 31–49

Wolfe, R. E., Roy, D. P., & Vermote, E. (1998). MODIS Land Data Storage, Gridding, and Compositing Methodology: Level 2 Grid, *Geoscience and Remote Sensing, IEEE Transactions on*, *36*, 1324–1338

Xiong, X. & Barnes, W. (2006). *MODIS Calibration and Characterization*, chap. 5, (pp. 77–97), Springer Berlin Heidelberg

Zurita-Milla, R., Kaiser, G., Clevers, J., Schneider, W., & Schaepman, M. (2009). Downscaling time series of MERIS full resolution data to monitor vegetation seasonal dynamics, *Remote Sensing of Environment*, *113* (9), 1874–1885

List of Figures

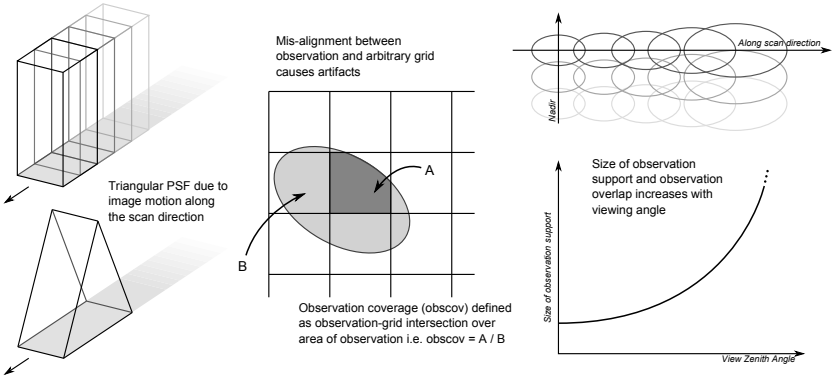

Figure 1: Effects contributing to the MODIS spatial response in the level 2 products: (left) the along scan image motion causes the squared detector point spread function (PSF) to become triangular when integrated during the time necessary to record one measurement; (centre) there is not a complete overlap between the observation footprint and the grid; and (right) the size of the observation support increases with the view zenith angle in the along scan direction.

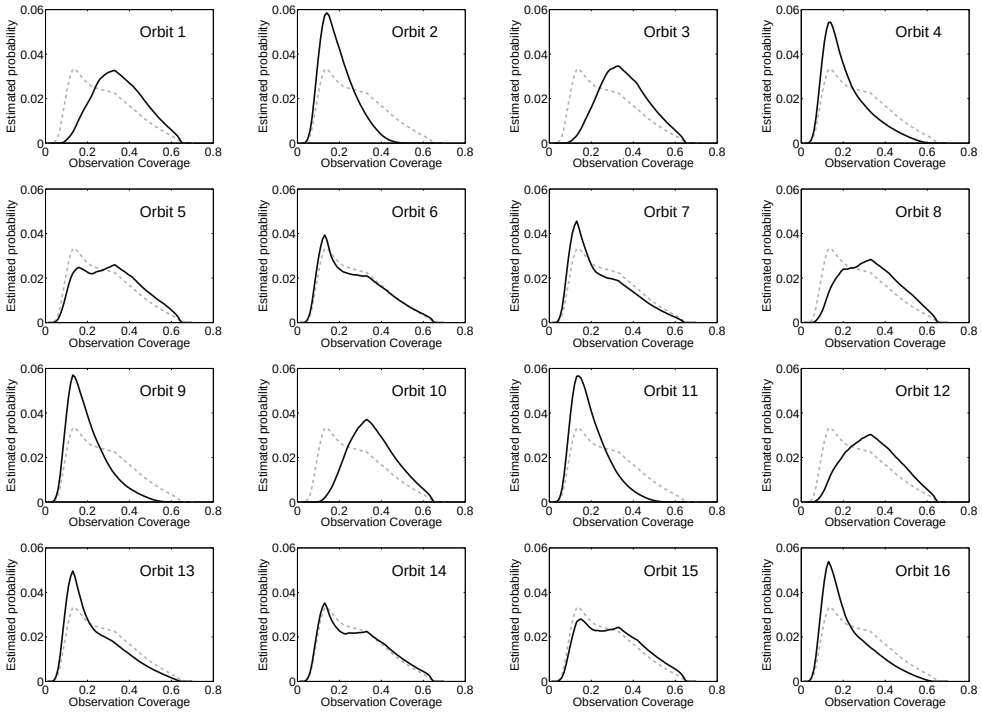

Figure 2: Estimated probability density functions of observation coverage (*obscov*) over the entire MODIS tile where the study site is located (tile H19V04) for each MODIS orbit. The sequence of the orbit numbers corresponds to the 16 consecutive days in the revisit cycle. On each subplot, the function of the given orbit (dark continuous line) can be compared to the mean observation coverage probability density function (light grey dashed line) covering the entire 16-day revisit cycle.

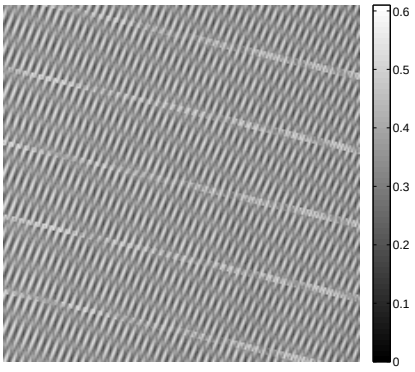

Figure 3: Example of the spatial variation of observation coverage (*obscov*) for a 200 × 200 pixel area. The value of *obscov* is displayed according to the grey scale

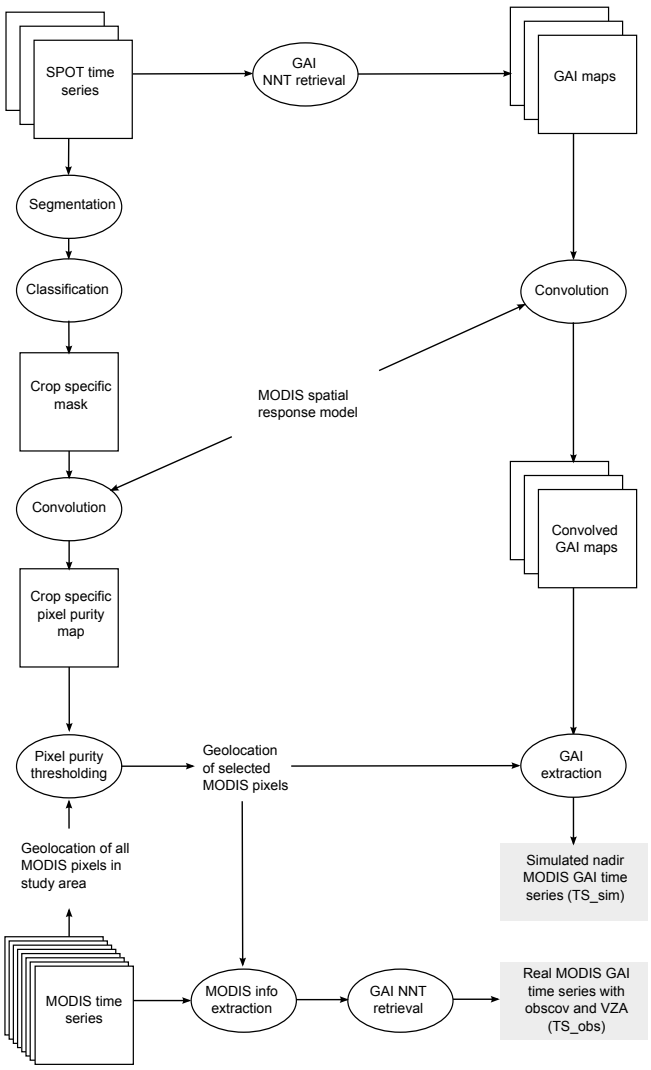

Figure 4: Flowchart to produce comparable GAI products from SPOT and MODIS imagery.

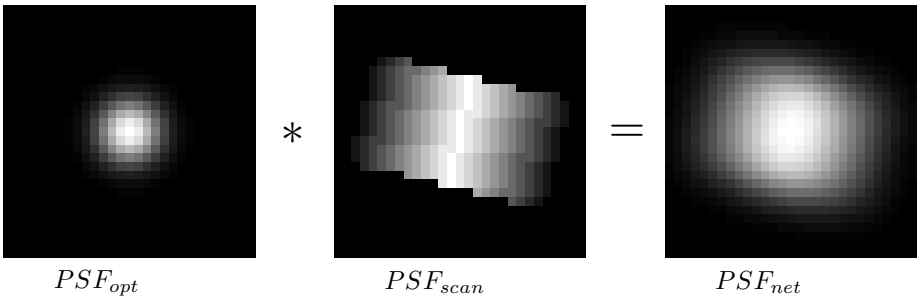

Figure 5: Schematic representation of the construction of the MODIS net point spread function based on the convolution of the optical with the scan PSF.

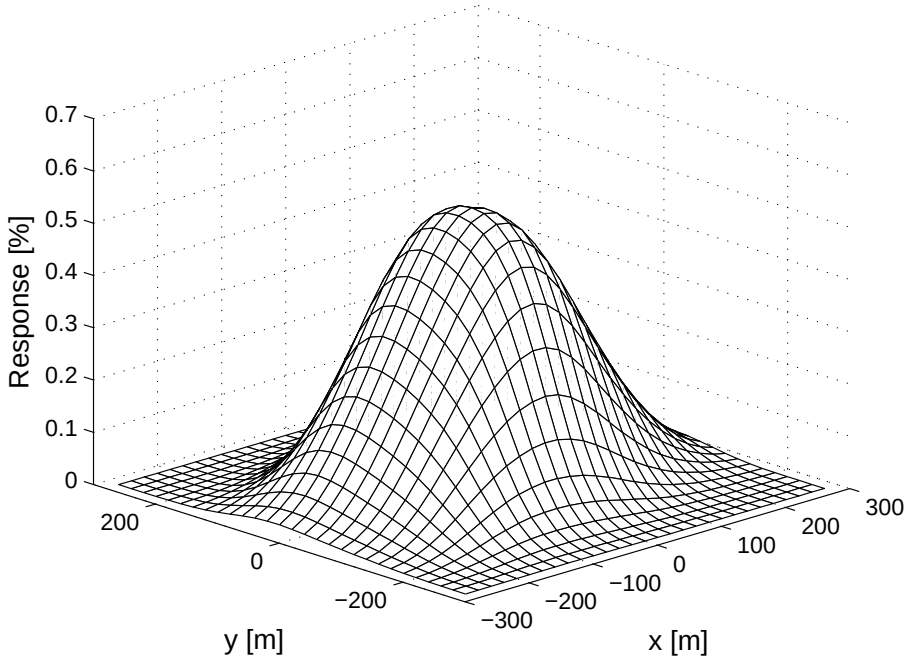

Figure 6: Spatial response (net point spread function) model of MODIS. Distances are calculated in meters from the centre of the observation footprint

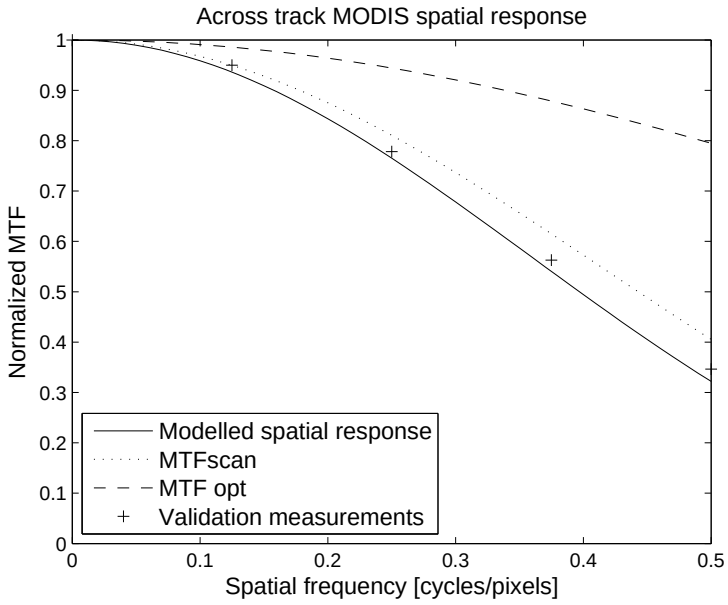

Figure 7: Comparison of the modelled spatial response of MODIS with MTF measurements realized by the MODIS calibration support team (http://mcst.gsfc.nasa.gov/).

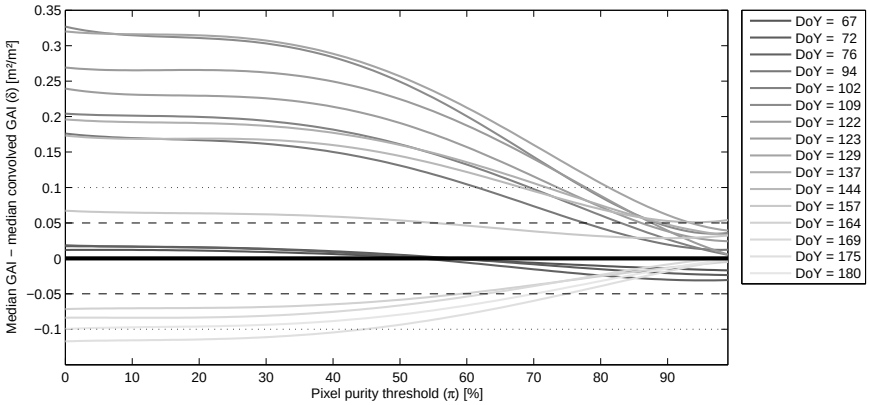

Figure 8: Effect of increasing pixel purity selection thresholds (π) on the difference (δ) between median GAI from the original GAI maps and the convolved GAI maps for different dates (represented in increasingly lighter shades of grey).

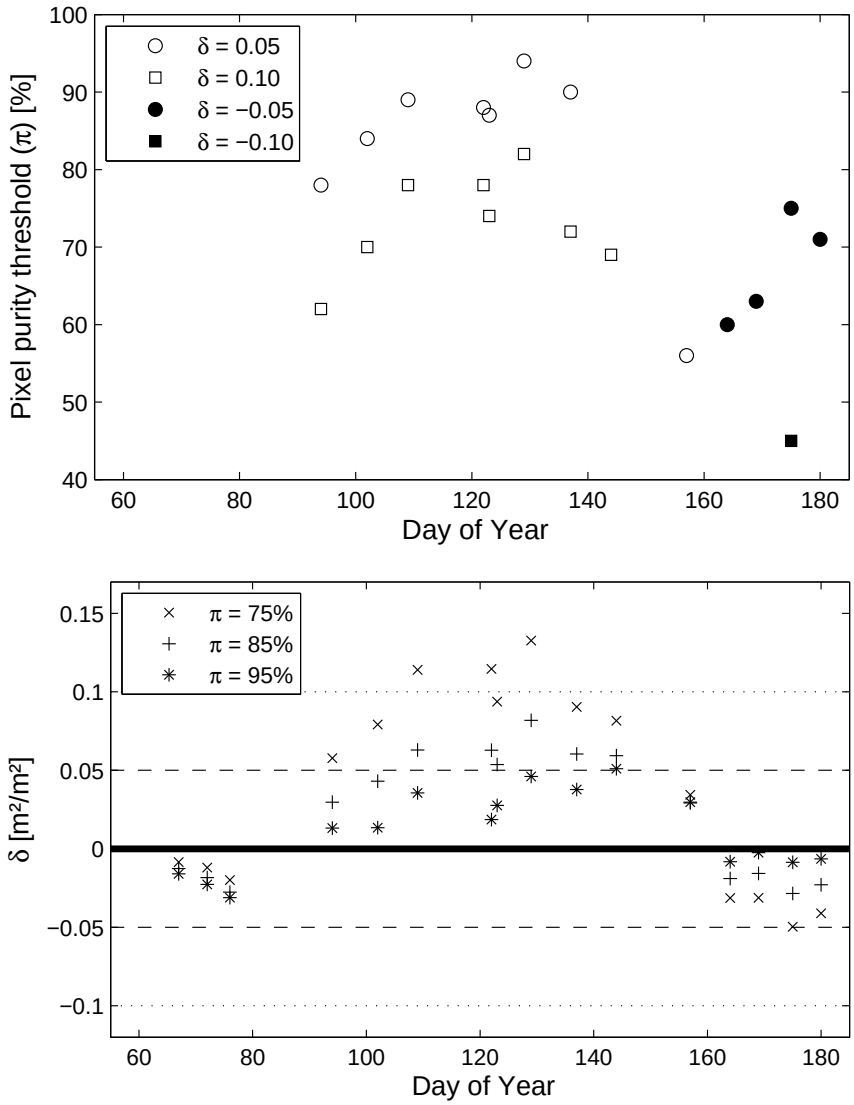

Figure 9: Evolution along the growing season of (top) the minimum acceptable pixel purity π and (bottom) the GAI bias δ for a given set of fixed conditions of respectively δ and π. Note that for the top figure, the number of points in each set can be different depending on the number of curves in figure 8 which cross the different δ thresholds.

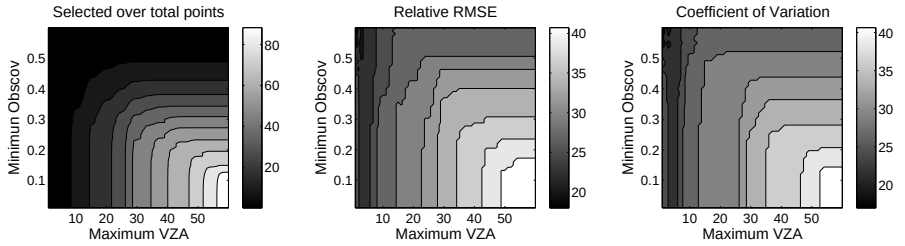

(a) (b) (c)

Figure 10: Combined effect of thresholds of a maximum VZA and a minimum *obscov* on (a) the percentage of estimations, (b) the relative RMSE and (c) the coefficient of variation between at nadir simulated MODIS time series and observed MODIS time series.

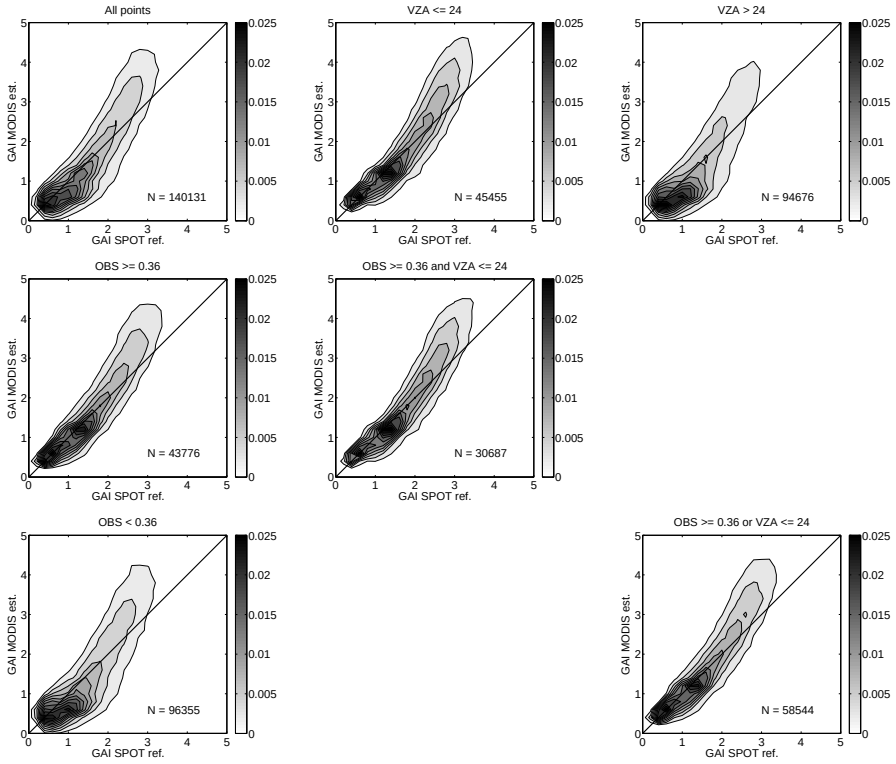

Figure 11: Comparison of the GAI values obtained from MODIS real values and temporally smoothed simulations of at nadir GAI based on SPOT high spatial resolution GAI maps. The contour plots of the 2-D distribution for all available points (top left) and for subsets according to VZA and *obscov* thresholds indicated above the figures.

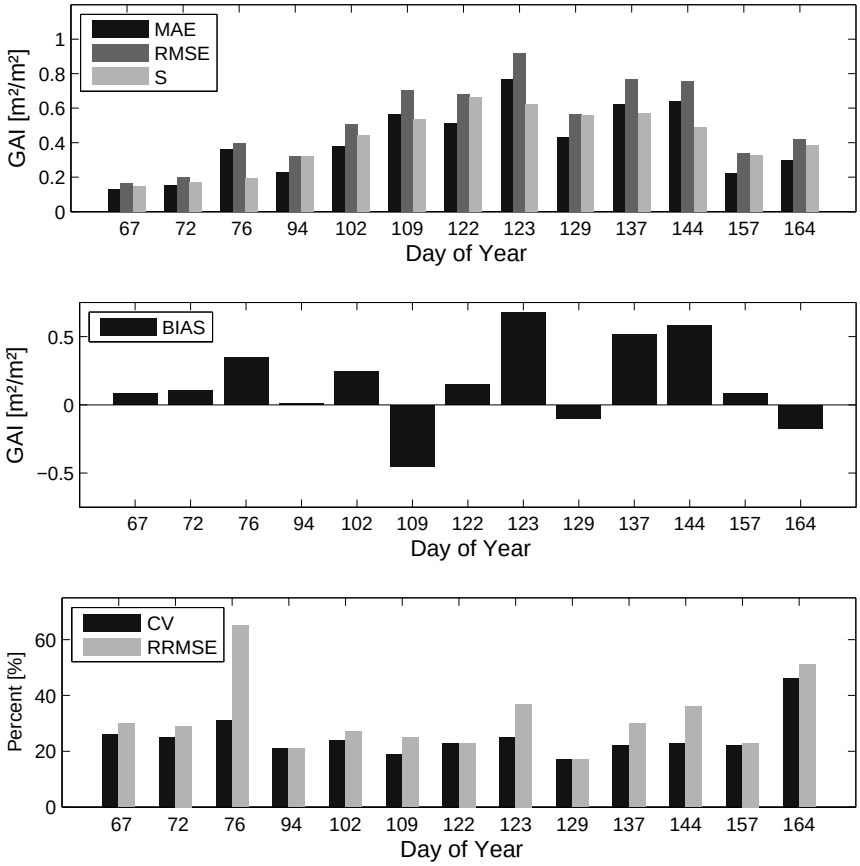

Figure 12: Statistical indicators comparing the performance of temporally smoothed MODIS GAI estimations against corresponding upscaled punctual SPOT GAI estimations. All MODIS points had a crop specific pixel purity (π) above 75%. The bias indicates the difference of MODIS estimations minus SPOT estimations.

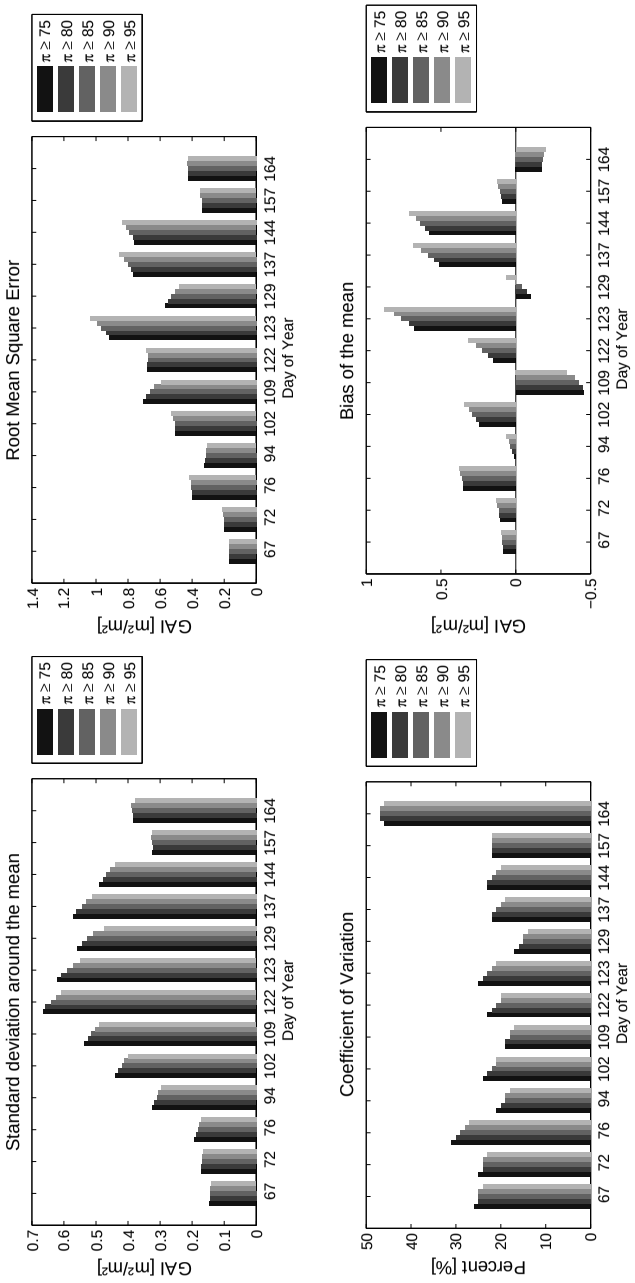

Figure 13: Statistical indicators comparing the performance of temporally smoothed MODIS GAI estimations against corresponding upscaled punctual SPOT GAI estimations for different pixel purity values

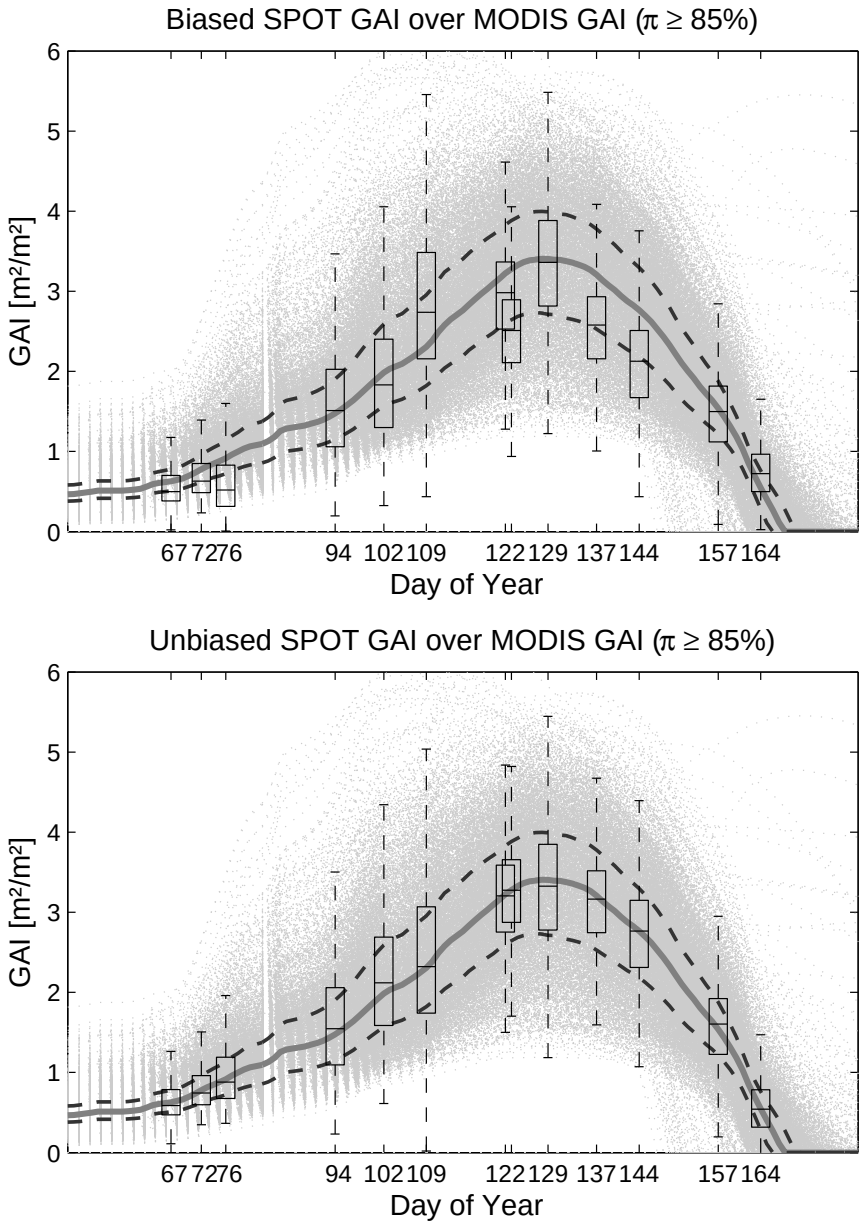

Figure 14: Boxplots of the SPOT GAI distributions overlayed over the ensemble of MODIS time series above 85% of crop specific purity. On top, the SPOT GAI distributions can be seen with their respective bias and on the bottom graph, the biased has been corrected. The solid line depicts the median value of MODIS time series, while the dashed lines represent the inter-quartile range (to be compared with the boxes).

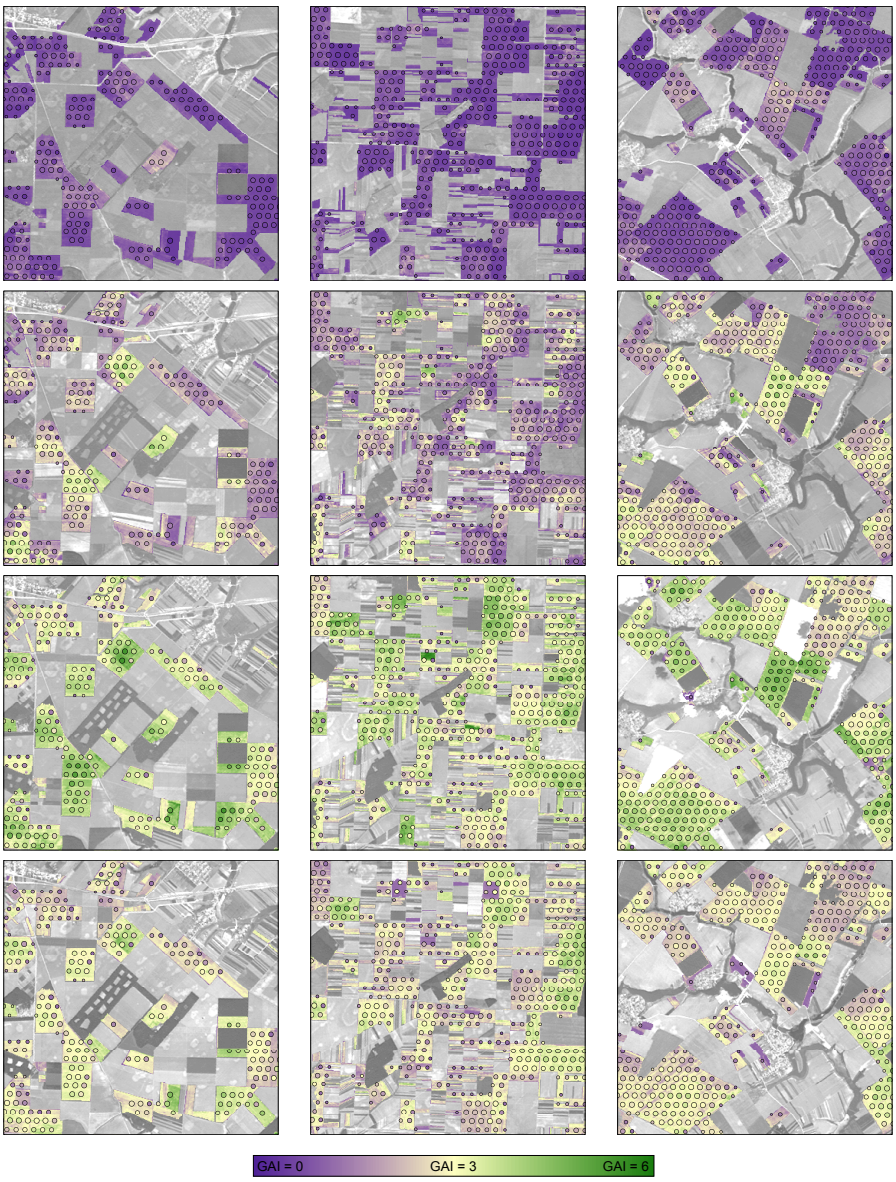

Figure 15: Spatial comparison between high spatial resolution GAI maps from SPOT (in the background) with MODIS GAI estimations (dots) for 3 different 7.2 × 7.2 km zones at the following days of year (from top to bottom): 76, 102, 123 and 144. The size of the dots relates to the pixel purity of the MODIS estimations, with larger dots being purer than smaller ones (only estimations above 75% pixel purity are shown). The images in the background are the respective Red channel of the original SPOT imagery used to derive the GAI maps.

List of Tables

Table 1: Details of the SPOT imagery used in this study to retrieve GAI. All images were acquired in 2001.

Date	DoY	Platform/Instrument	VZA	SZA	RAA
08–Mar	67	SPOT4/HRVIR2	19°	52.9°	-51.7°
13–Mar	72	SPOT4/HRVIR1	13°	50.7°	-52.5°
17–Mar	76	SPOT4/HRVIR2	19°	47.6°	-239.7°
04–Apr	94	SPOT2/HRV1	8°	41.6°	-52.7°
12–Apr	102	SPOT4/HRVIR1	20°	37.3°	-239.4°
19–Apr	109	SPOT4/HRVIR1	29°	37.3°	-45.2°
02–May	122	SPOT1/HRV1	20°	32.3°	-46.9°
03–May	123	SPOT4/HRVIR2	15°	30.3°	-236.5°
09–May	129	SPOT4/HRVIR2	8°	29.8°	-48.6°
17–May	137	SPOT1/HRV1	2°	27.5°	-49.8°
24–May	144	SPOT4/HRVIR2	9°	25.7°	-231.3°
06–Jun	157	SPOT1/HRV1	20°	23.2°	-234.3°
13–Jun	164	SPOT4/HRVIR2	30°	22.3°	-236.5°

Table 2: Statistics indicators and their definitions

Statistic	Formula
Mean Absolute Error	$MAE = \frac{1}{N}\sum_{i=1}^{N}\lvert\hat{z}_i - z_i\rvert$
Root Mean Square Error	$RMSE = \sqrt{\frac{1}{N}\sum_{i=1}^{n}\left(\hat{z}_i - z_i\right)^2}$
Bias	$B = \frac{1}{N}\sum_{i=1}^{N}\hat{z}_i - z_i$
Standard Deviation	$S = \sqrt{\frac{1}{N}\sum_{i=1}^{N}(\hat{z}_i - z_i - B)^2}$
Relative Root Mean Square Error	$RRMSE = 100 \times \frac{RMSE}{\bar{z}}$
Coefficient of variation	$\mathrm{CV} = 100 \times \frac{S}{\bar{z}}$

N: number of observations; $\hat{z}$: satellite estimations
z: ground measurements
$\bar{z}$: mean value of the ground measurements

Table 3: Effect that filtering out some GAI estimations, from the entire available dataset Z, has on temporal consistency of the GAI time series. Temporal consistency is evaluated by comparing the selected values to the CSDM results. The different cases analysed here are: the union of *obscov* and VZA constraints ($z_1 \subset Z : VZA \leq 24° \cup obscov \geq 0.36$), their intersection ($z_2 \subset Z : VZA \leq 24° \cap obscov \geq 0.36$) and a set of randomly selected individual GAI estimations (z_3) with the same sample size as z_1.

Case	**RMSE**	**RRMSE**	**B**	**S**	$\bar{n}$
Z	0.514	30.9%	−0.013	0.521	30.3
z_1	0.433	23.6%	−0.084	0.420	13.2
z_2	0.413	22.4%	−0.055	0.397	7.1
z_3	0.504	30.6%	−0.014	0.510	13.2
z_1†	0.355	19.2%	−0.020	0.361	13.2

† CSDM fitted on z_1 instead of on all Z points

Table 4: RMSE between the estimation of the percentiles of the high spatial resolution GAI distributions with the ensemble of coarse spatial resolution GAI time series when increasingly harsh levels of pixel purity are selected to threshold the latter. In bold is the lowest RMSE for estimating a given percentile.

Percentiles	**Pixel purity threshold**				
	75%	80%	85%	90%	95%
2.5%	**0.234**	0.241	0.253	0.278	0.282
25%	0.161	0.137	0.109	0.087	**0.079**
50%	0.077	0.059	**0.053**	0.064	0.083
75%	0.140	**0.139**	0.144	0.144	0.149
97.5%	0.365	**0.362**	0.364	0.366	0.369